RSC Advances

PAPER

View Article Online
View Journal | View Issue

Cite this: *RSC Adv.*, 2019, **9**, 766

Dopamine-derived cavities/Fe_3O_4 nanoparticles-encapsulated carbonaceous composites with self-generated three-dimensional network structure as an excellent microwave absorber†

Lin Guo,[a] Sheng-Shuai Gao,[a] Qing-Da An,*[a] Zuo-Yi Xiao,[a] Shang-Ru Zhai,*[a] Dong-Jiang Yang*[b] and Li Cui[a]

Dopamine-derived cavities/Fe_3O_4 nanoparticles-encapsulated carbonaceous composites with self-generating three-dimensional (3D) network structure were successfully fabricated by a facile synthetic method, in which sodium alginate provided carbon matrix pores and excellent microwave absorption performance was established. The hollow cavities derived from the core–shell-like $CaCO_3$@polydopamine were creatively introduced into the 3D absorber to significantly improve the absorption performance. The sample calcined at 700 °C exhibited the most outstanding microwave absorption performance, with minimal reflection loss up to −50.80 dB at 17.52 GHz with a rare thickness of only 1.5 mm when filler loading was 35% in paraffin matrix. The effective absorption bandwidth of reflection loss < -10 dB reached 3.52 GHz from 14.48 GHz to 18 GHz, corresponding to the same thickness of 1.5 mm. In contrast, the sample without hollow dopamine-derived cavities showed poor performance due to poor impedance matching, and this highlights the role of hollow cavities brought into the 3D structure, which led to a difference in interfacial polarization, multiple reflections and scattering. The novel dopamine-derived cavities/Fe_3O_4 nanoparticles-encapsulated carbonaceous composites with 3D network structure can be regarded as a promising candidate for application as a microwave absorber with strong absorption.

Received 25th October 2018
Accepted 18th December 2018

DOI: 10.1039/c8ra08851a

rsc.li/rsc-advances

Introduction

In the 21st century, the issue of environmental pollution has entered a white-hot stage, in which air pollution, water pollution and other forms of pollution have drawn more attention as compared with the electromagnetic pollution produced by new technology. However, with the rapid development of electrical communication equipment, microwave pollution is becoming more and more serious, leading to many health problems for human beings.[1,2] Additionally, electromagnetic interference (EMI) often causes a non-negligible trouble in military fields.[3,4] Therefore, the development of some high-performance microwave absorption materials for eliminating the great threat of microwaves is quite urgent. An ideal microwave absorber is generally expected to induce the maximum microwaves into the absorber and then transform it into other energy such as heat. What is universally accepted is that an excellent absorber should display the following essential features in practical applications: lightweight, thin, broad absorption band and strong absorption on booting.[5]

Recently, lightweight carbon-based materials have been widely used as microwave absorption materials due to the controllability of their micromorphology and chemical compositions. For example, carbon nanotubes (CNT), one-dimensional nanomaterials whose hexagonal structures are perfectly connected, have become a hot topic as microwave absorbers. Some reports have focused on decorating CNT with magnetic or dielectric components to enhance the absorption performance,[6,7] while others combined the CNT or multiwall CNT (MWCNT) with other components to form composites directly.[8,9] Nevertheless, almost all of the CNT or MWCNT used in microwave absorption originate from costly commercial products, which might significantly restrict their large-scale applications. Other popular carbon-based materials developed for microwave absorption are graphite derivatives, namely, graphite oxide and graphene oxide.[10–12] Despite their absorption performance, the preparation process, in which the classical or modified Hummers' method is usually adopted, is time-consuming and inevitably involves environmentally toxic byproducts, including concentrated acids and heavy metal ions.[13,14]

---

[a] *Faculty of Light Industry and Chemical Engineering, Dalian Polytechnic University, Dalian 116034, P. R. China. E-mail: anqingdachem@163.com; zhaisrchem@163.com*

[b] *Collaborative Innovation Center for Marine Biomass Fibers Materials and Textiles of Shandong Province, School of Environmental Science and Engineering, Qingdao University, Qingdao 266071, P. R. China. E-mail: d.yang@qdu.edu.cn*

† Electronic supplementary information (ESI) available. See DOI: 10.1039/c8ra08851a

Biomass-derived carbon (BDC) has emerged as an environmentally friendly and resource-saving material that has been successfully used in many fields. For instance, it has been used as battery cathodes,[15] water pollutant absorber,[16] supercapacitor electrodes[17] and so on. To date, there have been extensive applications of this material *via* component optimization and/or structural control due to its natural characteristics like porous structure, abundant doped heteroatoms and stable network. In addition, BDC has stood out as a microwave absorbing material in recent years. Xu and Gao both developed efficient microwave absorbers with honeycomb-like carbon derived from natural walnut shell, in which the porous structure played a key role in microwave attenuation and impedance matching.[18,19] Singh and coworkers used the interesting chicken feather fibers to fabricate heteroatom-doped carbon without additional magnetic materials; the presence of nitrogen in the feathers helped to naturally attain doped carbon and an excellent microwave absorber with numerous defects, interfaces and 3D porous structure was obtained.[20] In contrast to the published porous/network structure that comes from the chemical synthesis,[21] this special structure originating from biomass is innate and the preparation process is green, low-energy and time-saving. However, the exploration of a more sustainable strategy to fabricate 3D carbonaceous composites with tailored network nanostructures, even dispersion of magnetic species, doped-heteroatoms and up-scale production processes is of practical significance for meeting the requirements of potential microwave absorbers.

Herein, sodium alginate (SA), a biomass material derived from seaweed, has been explored for the fabrication of a carbonaceous microwave absorber with 3D network structure *via* a simple preparation process. SA contains masses of hydroxyls and carboxyls that can help easy gelation under extremely mild conditions. More notably, compared with other reports involving chemical synthesis by organics, or complicated activating/etching processes on the biomass,[18,22] the formed gel material maintains a self-generating and inartificial 3D network structure, which leads to numerous heterogeneous solid–void interfaces after freeze-drying and calcination. Such special hierarchical architectures, also including sponge-like structures[23] and flower-like structures,[24] have always been pursued by researchers in this fascinating field. The solid–void interfaces can generate interfacial polarization, multiple reflections and scattering in the presence of microwaves and then attenuate the microwaves.[25,26] Nevertheless, there are limited reports on microwave absorption by SA. Moreover, Fe^{3+} can be cross-linked with alginate macromolecules when SA gels and subsequently, magnetic Fe_3O_4 nanoparticles that make a significant contribution to magnetic dissipation will be generated *in situ* during the carbonization process. Another crucial composition in our composites is the hollow cavities derived from preformed core–shell-like $CaCO_3$@polydopamine, which endow the resultant composites with numerous defects, interfaces and 3D porous structures. As reported, dopamine can oxidize and spontaneously polymerize on any particle surface to eventually form polydopamine.[27] Hydroxyl and amino groups in dopamine not only serve as a key factor in the polymerization process but also cause many defects during carbonization. These defects and the hollow structure cause defect polarization, electric or dipolar polarization, interfacial polarization, multiple reflection and scattering, all of which can result in a higher minimum reflection loss.[28] Furthermore, the hydroxyls on the polydopamine surface will chemically combine with the carboxyls of SA to ensure the stability of the compositions when gelling. Profiting from the synergistic effect of the SA-derived carbonaceous matrix, hollow dopamine-derived cavities and Fe_3O_4 nanoparticles, the as-fabricated composites exhibited eye-catching microwave absorption performance with minimal reflection loss of −50.80 dB and filler loading of 35% at a 1.5 mm thickness. Moreover, the effective absorption bandwidth of reflection loss < -10 dB could reach 3.52 GHz corresponding to the same thickness of 1.5 mm. So far, the feasible strategy of taking advantage of the hollow dopamine-derived cavities and the carbonaceous 3D network structure combined still needs to be investigated. This could possibly make a significant contribution to the design and synthesis of high-performance microwave absorption materials, and the novel dopamine-derived cavities/Fe_3O_4 nanoparticles-encapsulated carbonaceous composites with 3D network structure would be a remarkable candidate as microwave absorber.

Experimental section

Materials

Sodium alginate ($(C_6H_7NaO_6)n$, SA) was purchased from Tianjin GuangFu Fine Chemical Research Institute. Dopamine hydrochloride ($C_8H_{11}NO_2$–HCl), tris(hydroxymethyl)aminomethane ($C_4H_{11}NO_3$, Tris) and calcium carbonate ($CaCO_3$, electronic grade) were purchased from Aladdin Industrial Co. Ltd. Hydrochloric acid (HCl) was purchased from Kermel. Iron chloride hexahydrate ($FeCl_3 \cdot 6H_2O$) and ethanol (CH_3CH_2OH) were purchased from Sinopharm Chemical Reagent Co. Ltd. All the chemical reagents used in this work were of analytical grade and were used without further purification.

Preparation of hollow dopamine-derived cavities

Pre-determined 0.4 mol Tris, 2 g $CaCO_3$ and 1 g dopamine hydrochloride were added to 400 mL distilled water and then stirred slowly at room temperature for 24 h. At this stage, the dopamine could oxidize and self-polymerize on the surface of $CaCO_3$ particles and ultimately form a compact layer. After that, the resulting slurry was vacuum filtered, and the filter cake was dried under vacuum at 60 °C for 12 h, then the grayish black $CaCO_3$@polydopamine powder was obtained and denoted as CPDA, in which the hard template $CaCO_3$ had not been removed. The encapsulated hollow dopamine-derived cavities without $CaCO_3$, denoted as HDC, appeared when the final sample underwent subsequent carbonation and pickling.

Preparation of hollow dopamine-derived cavities/Fe_3O_4 nanoparticles-encapsulated carbonaceous composites

CPDA (2 g) and SA (2 g) were added to 100 mL of distilled water successively and stirred vigorously for 12 h to obtain a homogeneous colloidal mixture, then the acquisition was added dropwise to 1% $FeCl_3$ (w/v) solution for crosslinking to form SA–CPDA–Fe(III) hydrogel spherules and left undisturbed in Fe(III) solution for 6 h to guarantee complete crosslinking. The hydrogel spherules were washed with distilled water and ethanol to remove redundant Fe^{3+} and Cl^{-1} ions. Then, these spherules were transferred into a freezer at −50 °C for 10 h and dehydrated *via* the freeze-drying method in a vacuum freeze dryer for 10 h to obtain dried SA–CPDA–Fe(III) spherules.

The dried SA–CPDA–Fe(III) spherules were calcined in a tube furnace with the heating rate of 5 °C min^{-1} to a set temperature (700, 800 or 900 °C) for 2 h in N_2 atmosphere. After being cooled to room temperature, the obtained materials were washed with HCl solution (pH 4) and distilled water several times until neutral and then dried at 60 °C. In this specific acidic solution, the content of magnetic Fe_3O_4 would not be damaged and CaO or $CaCO_3$ could be effectively removed; the HDC was formed in the finished product. The as-prepared samples were ground into powder and named HFC-*X* (X = 700, 800 or 900 °C), based on the employed heating temperature. For comparison, FC-700 was also treated with the same procedure as HFC-700, without adding HDC. The manufacturing process of HFC-700 is illustrated in Scheme 1.

Characterization

Phase analysis was performed by powder X-ray diffraction (XRD, Bruker D8 Advance) with Cu-K_α radiation ($\lambda = 1.540$ Å) at 40 kV over the angular range from 10° to 80°. The morphologies of the samples were investigated by field-emission scanning electron microscopy (SEM, JEM JEOL 2100) and transmission electron microscopy (TEM, Hitachi H9000NAR), respectively. The surface properties were characterized by X-ray photoelectron spectroscopy (XPS, ESCALAB210) and Brunauer–Emmett–Teller (BET, JW-BK222) methods *via* nitrogen adsorption and desorption measurements. Raman spectra were obtained *via* Raman microscopy (Renishaw PLC). A thermogravimetric analyzer (TG, Q50) was employed to test the thermal stability with the temperature increasing from 25 °C to 900 °C at a rate of 10 °C min^{-1}. The magnetic properties of the as-made composites were measured by a vibrating sample magnetometer (VSM, Lake Shore 7400) at room temperature.

Electromagnetic parameters were obtained by a vector network analyzer (Agilent N5224A) at room temperature. The prepared samples, mixed with paraffin with a filler content of 35%, were pressed into tori ($\Phi_{out} = 7.0$ mm, $\Phi_{in} = 3.04$ mm), and the complex permittivity and permeability values were measured in the 2–18 GHz range with a coaxial line method.

Results and discussion

Fig. 1 shows the representative SEM images of as-prepared samples. From Fig. 1(a–c), there is a clear 3D porous and continuous network structure, and the HDC can be seen everywhere in the heterarchical network. In Fig. 1(c) with high magnification, several nanoparticles (marked by red circles) of Fe_3O_4 can be seen in the void or wall of the network structure. Fig. 1(d) exhibits the same network structure of FC-700, in which the HDC was not introduced during fabrication. Fig. (1e)

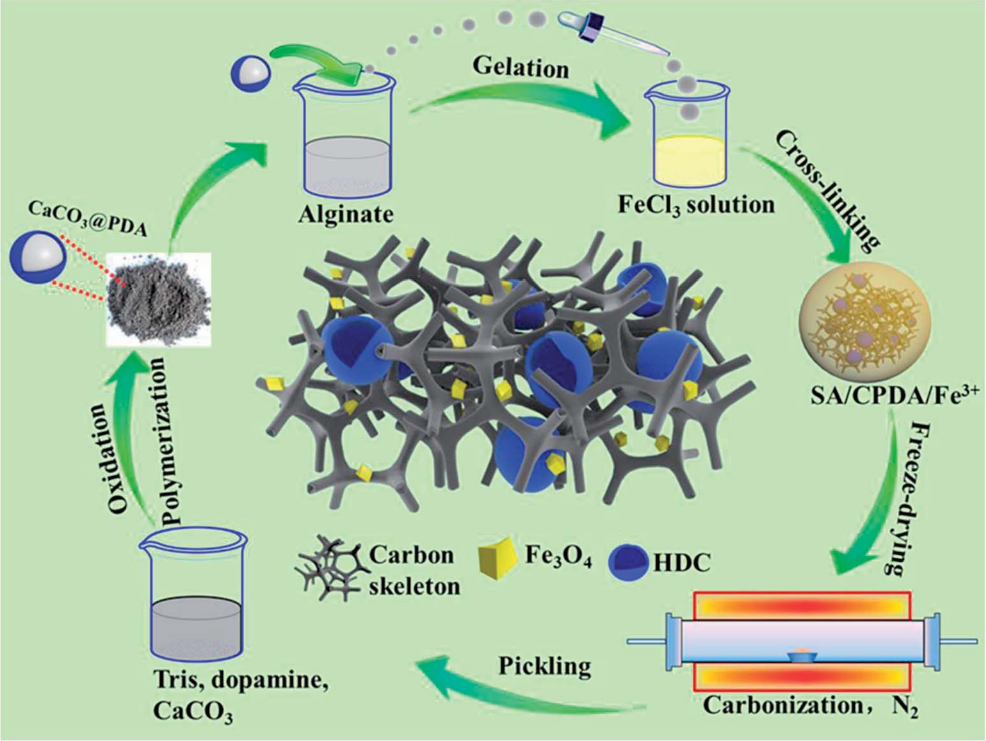

Scheme 1 Illustration of the possible preparation procedures of the HFC-700 composite.

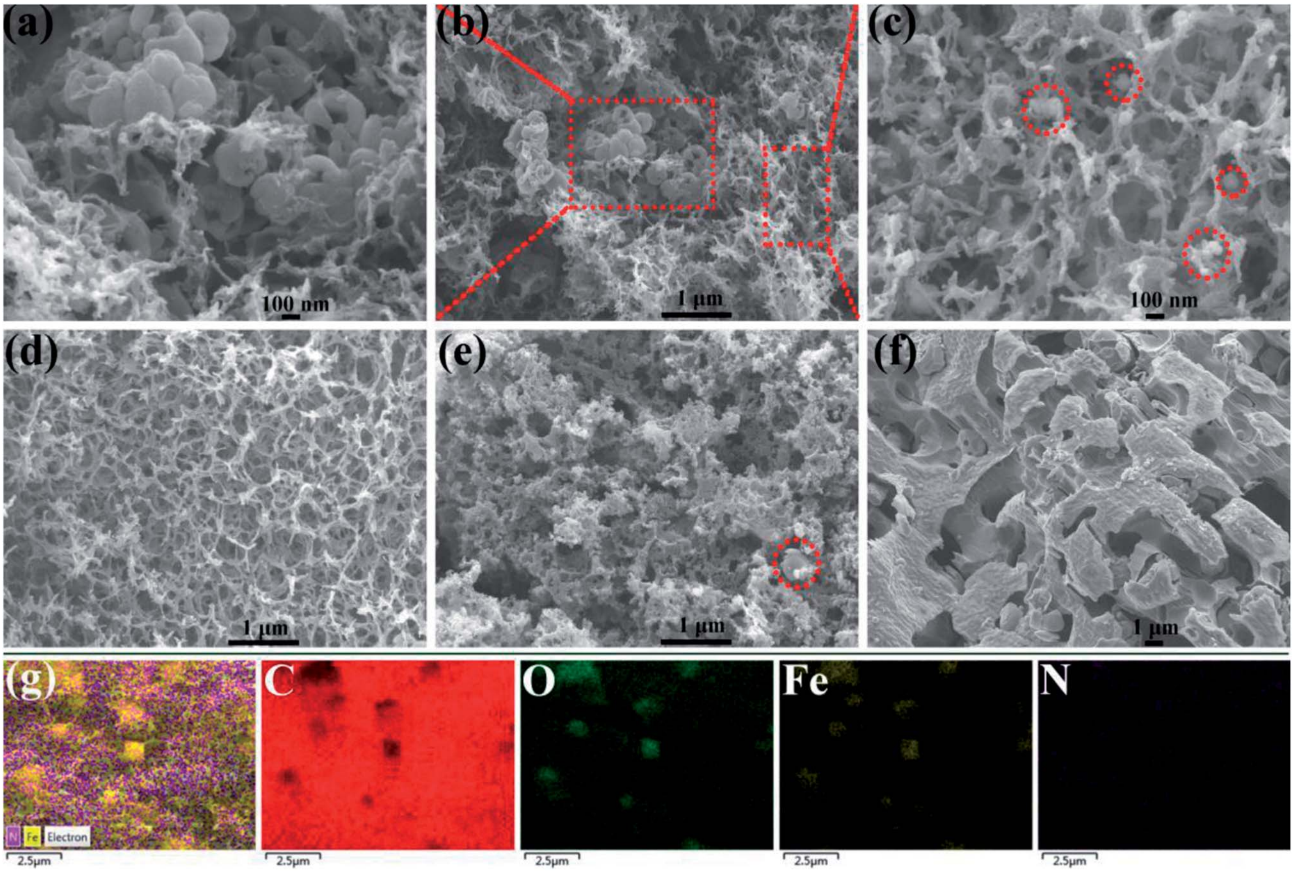

Fig. 1 SEM images of samples (HFC-700 (a–c) at different magnifications, FC-700 (d), HFC-800 (e), HFC-900 (f)) and elemental mapping of C, O, Fe and N for HFC-700 (g).

presents the morphology of HFC-800; the network structure aggregated and collapsed as compared with HFC-700, and the HDC (marked by a red circle) are few. Fig. 1(f) demonstrates a coked and nubby morphology of HFC-900, and no HDC is observed. Generally speaking, this transformation resulted from the increase in the carbonization temperature. Fig. 1(g) presents the elemental mappings of C, O, Fe and N for HFC-700. Remarkably, the N element content is relatively less as compared with others, and it came from the exclusive nitrogen source, that is, the trace amount of $-NH_2$ of polydopamine in dopamine-derived cavities. As we all know, only one $-NH_2$ exists in a dopamine molecule, besides, the cavities derived from dopamine served as one of the ingredients in of the large carbonaceous matrix. During thermal decomposition, N element partially spilled over or diffused into the carbon matrix, and for this reason, the outlines of these cavities did not emerge in the N elemental mapping.

Further details of morphologies and microstructure are shown in TEM images. Fig. 2(a–c) illustrates the Fe_3O_4 crystal particles and the HDC in HFC-700. The size distribution of particles (Fig. S1†) calculated from Fig. 2(a) by software shows that the Fe_3O_4 nanoparticles were mostly 50–80 nm in size, and the images with different magnifications (Fig. 2(a–c)) show that Fe_3O_4 nanoparticles were uniformly decorated on the SA-derived carbonaceous skeleton without aggregation and large vacancies. Compared to the SA-derived carbon, the skeleton of HDC can be clearly and easily seen, indicating that the HDC became ordered with a high degree of graphitization after carbonization, while the amorphous SA-derived carbonaceous matrix became more disordered with more defects. Separated SEM and TEM images of individual HDC, which was not brought into the carbonaceous matrix, are shown in Fig. S2.† Interestingly, some carbon shells that could provide extra interfaces surrounding the Fe_3O_4 crystal are also found in Fig. 2(c). This could be due to partial Fe^{3+} playing a role in catalytic crystallization of the carbon matrix during the carbonization process. Fig. 2(d) of FC-700 shows the Fe_3O_4 crystal particles only. The SAED pattern and magnified HRTEM image of Fe_3O_4 in HFC-700 are shown in Fig. 2(e and f). The sample possesses a higher crystallinity, which was confirmed by bright and distinguishable diffraction spots in array, and the diffraction spots can be indexed to the (111), (222), (220), (331) and (440) lattice planes according to the XRD results, illustrating the formation of the structure belonging to Fe_3O_4 (fcc). Fig. 2(f) clearly demonstrates the formation of lattice fringes with an interplanar distance of 2.97 Å, which agrees with the (220) plane of Fe_3O_4.

Superimposed XRD patterns in a close inspection of HFC-*X* and FC-700 were further examined and the results are presented in Fig. 3(a). The diffraction peaks in all tested composites are

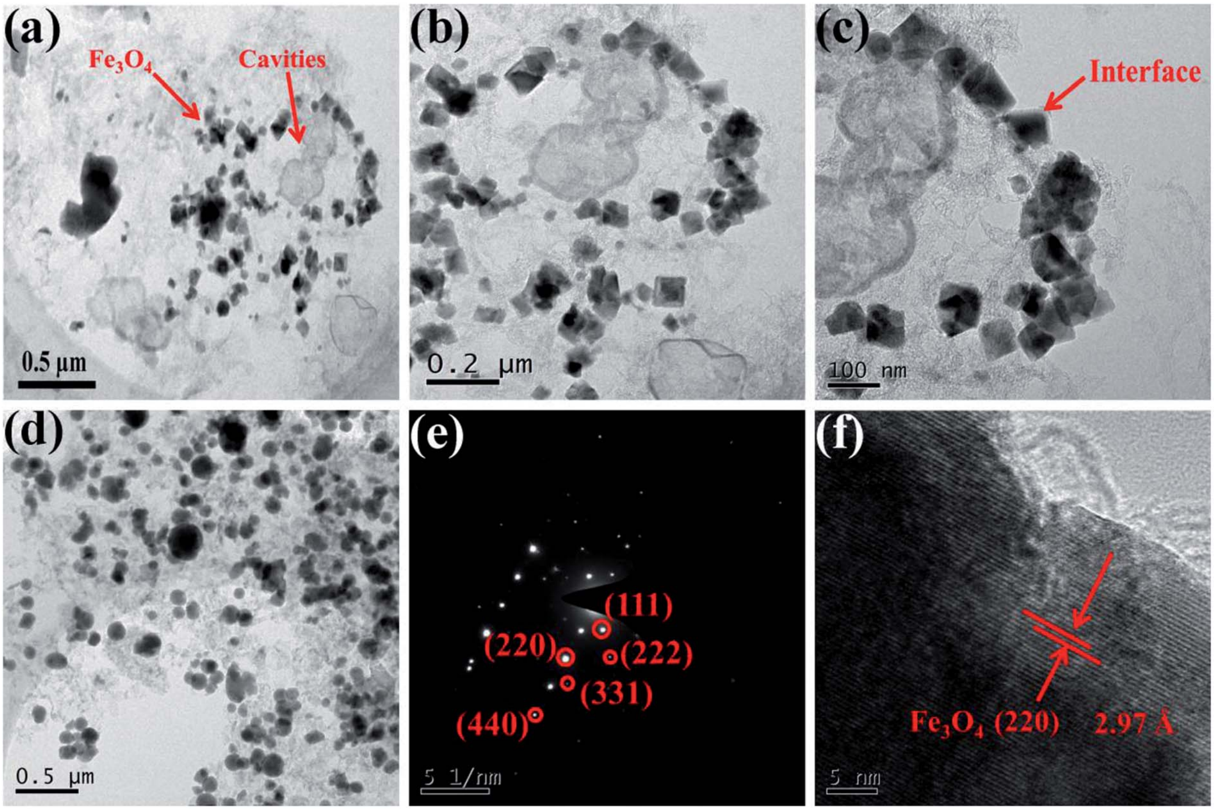

Fig. 2 TEM images of HFC-700 (a–c) with different magnifications and FC-700 (d), SAED images (e) and HR-TEM (f) of Fe_3O_4 crystals in HFC-700 hybrids.

centered at ∼18.3°, 30.1°, 35.4°, 37.1°, 43.1°, 47.2°, 53.4°, 57.0°, 62.6° and 65.8°, matching well to the (111), (220), (311), (222), (400), (331), (422), (511), (440) and (531) lattice planes of Fe_3O_4 in the fcc spinel phase (ICSD 85-1436). The sharp characteristic peaks detected above reveal a higher crystallinity of Fe_3O_4 in as-prepared samples, coinciding with TEM analysis. The appearance of a broad and weak peak at ∼15°–28° in all samples is due to the (002) crystal plane of hexagonal graphite (ICSD 75-1621) derived from SA and HDC.[29] It should be pointed out that no other impurity peaks were detected in the patterns and the phase purity can be clearly confirmed.

The structural changes in the carbon framework were further investigated using Raman spectra (Fig. 3(b)). All the spectra of the tested samples have two strong peaks around 1340 and 1590 cm^{-1}, in accord with the D-band (A_{1g} carbon vibration modes) and G-band (E_{2g} carbon vibration modes), respectively.[30] The strong D-band is normally associated with lattice defects in disordered carbon aroused by vacancies, heteroatoms, crystal boundaries or other defects, while the G-band is an in-plane stretching vibration mode of the sp^2-bonded carbon. The area ratio of these two bands (I_D/I_G) is a common indicator of the disorder degree, and its increasing value manifests the formation of defects.[31] The I_D/I_G values were calculated to be 0.15, 1.72, 1.70, 1.76 and 1.68 for samples HDC, FC-700, HFC-700, HFC-800 and HFC-900, respectively. The tested HDC, derived from CPDA that calcined at 700 °C and then treated with pickling, was not encapsulated by the carbonaceous matrix and was separately characterized by Raman. Notably, the I_D/I_G value of HDC is only 0.15, revealing a relatively high graphitization with fewer defects, whereas other complex carbonaceous samples have more defects with greater disorder. This is why the carbon skeleton coming from HFC rather than SA could be clearly seen in TEM images. Compared with FC-700, the HFC-700 exhibiting a slightly lower I_D/I_G ratio is probably due to the HFC in the composites. Those carbonaceous composites FC-700 and HFC-*X* all present noticeable I_D/I_G values (>1.6) in comparison to other carbon-based microwave absorption materials reported in related papers.[26,28,32] A high value that means more defects in the carbon is likely to largely inspire defect and dipole polarization, which give rise to the absorption properties.

Furthermore, on increasing the temperature, the I_D/I_G values of the HFC-*X* series show a significant variation. The highest I_D/I_G value (1.76) showed by HFC-800 is attributed to the pyrolyzation and activation of $CaCO_3$ in CPDA. The decomposition of $CaCO_3$ is accompanied by the release of CO_2, which further reacts with carbon atoms, and this effect enlarges the pores or creates new pores followed by more defects.[33] In contrast, HFC-900 exhibits the lowest value of I_D/I_G; the severe collapsing and coking of the carbon skeleton during calcination at 900 °C played a crucial role, despite the activation of $CaCO_3$ at 800 °C. Thermogravimetric analysis (TGA) curves show the thermal stability behavior of the $CaCO_3$, CPDA and dried SA–CPDA–Fe(III) composites in Fig. 3(c). All three samples exhibit a sharp

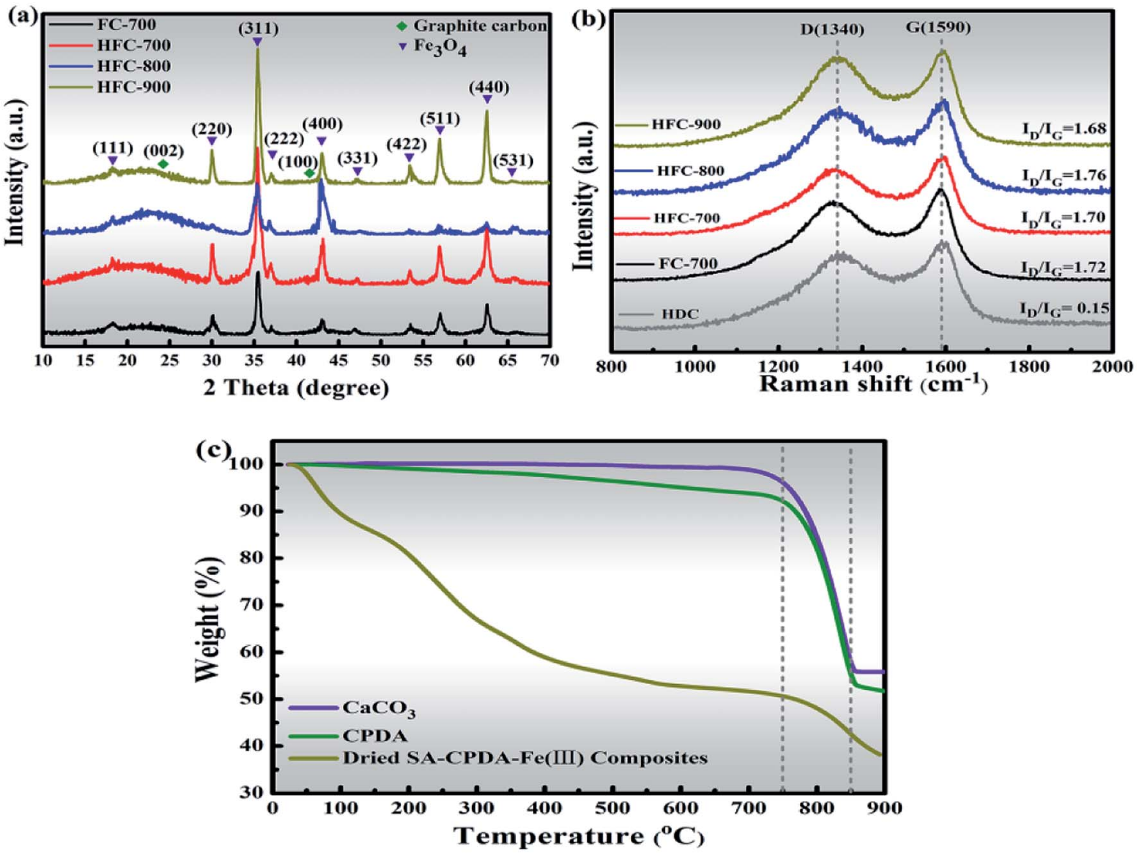

Fig. 3 XRD patterns of HFC-*X* and FC-700 (a), Raman spectra of HFC-*X*, FC-700 and HNC (b) and TGA curves of $CaCO_3$, CPDA and dried SA–CPDA–Fe(III) composites (c).

weight loss at about 800 °C, coinciding with the thermal-decomposition of $CaCO_3$, and this is consistent with the foregoing Raman analysis. Specifically, for the dried SA–CPDA–Fe(III), there is a drastic downward trend before 200 °C, which was caused by the removal of water. In the temperature range of 200–750 °C, the weight loss is mainly attributed to the pyrolysis of the SA-based matrix, and also includes the thermal decomposition of the dopamine-derived cavities.

Additionally, the characteristics of the porous structures of samples were investigated by N_2 adsorption–desorption isotherm measurement, and the curves are depicted in Fig. 4. All the samples possess similar variations with a characteristic hysteresis loop. These isotherms belong to the type IV isotherm according to the IUPAC classification. The hysteresis loop in these isotherms indicates that these samples possess abundant mesopores.[34] The specific surface area (S_{BET}), total pore volume and the most probable pore size (W_{peak}) of the samples are presented in Table S1.† As for S_{BET} and total pore volume, there are no significant differences between FC-700 and HFC-700, yet HFC-800 showed itself in HFC-*X* series due to the pyrolyzation and activation of inner $CaCO_3$ at around 800 °C. This emphasizes the regulatory function of pores by $CaCO_3$ in carbon-based materials. The main reason for the distinct decrease in S_{BET}, total pore volume and W_{peak} of HFC-900 may be the collapse and structural coking of the pore canals, which are in accord with SEM and TGA investigations.

Further studies by XPS on elemental states and chemical compositions are shown in Fig. 5. The wide-scan spectra of FC-700, HFC-700, HFC-800 and HFC-900 are presented in Fig. 5(a). Three characteristic peaks of Fe, O and C elements can be clearly observed in all spectra belonging to FC-700, HFC-700,

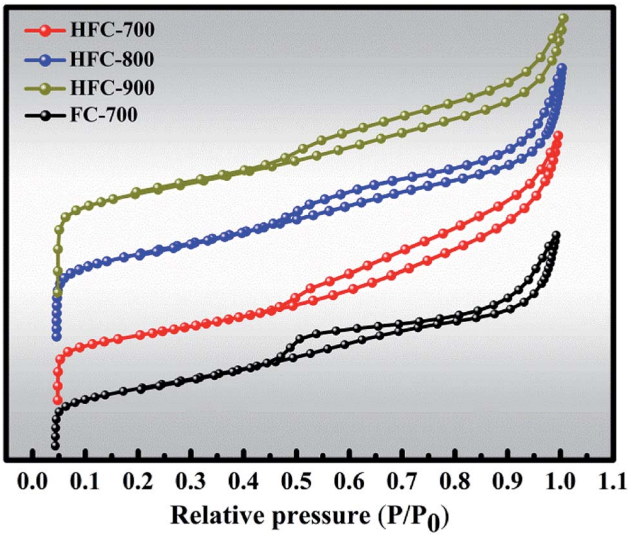

Fig. 4 Nitrogen adsorption–desorption isotherms of as-prepared samples.

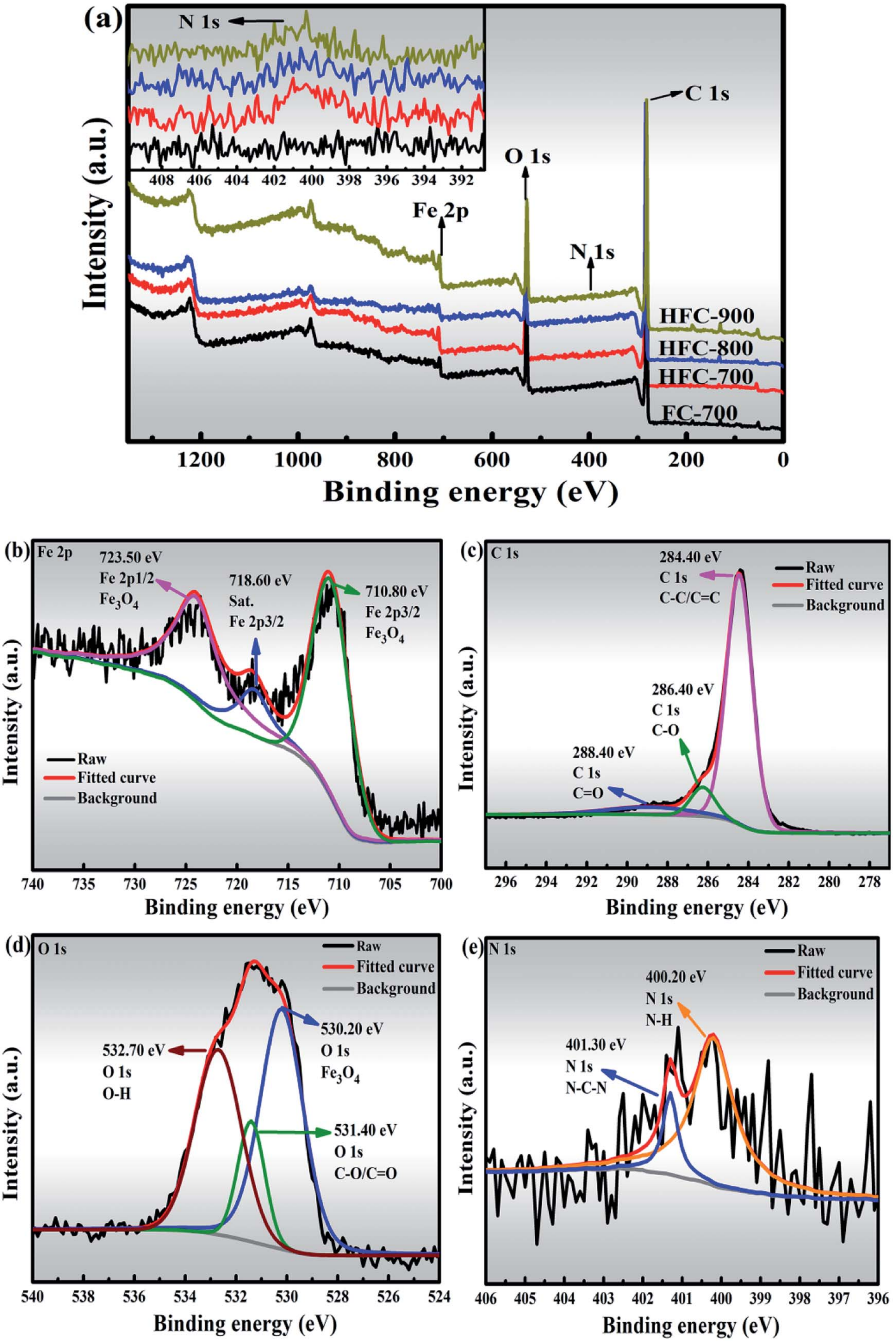

Fig. 5 XPS spectra (wide-scan spectra of FC-700, HFC-700, HFC-800 and HFC-900 (a), Fe 2p spectrum of HFC-700 (b), C 1s spectrum of HFC-700 (c), O 1s spectrum of HFC-700 (d), N 1s spectrum of HFC-700 (e)).

HFC-800 and HFC-900, respectively. It must be pointed out that the characteristic peaks of N element are significantly weak or even nonexistent in the spectra of all tested samples (shown in the magnified inset of Fig. 5(a)). The N elements in HFC-700 (1.85 at%), HFC-800 (1.49 at%) and HFC-900 (1.09 at%) come from polydopamine, which ultimately constructs HDC, whereas there is no N element in FC-700. The decrease of N element in HFC-700, HFC-800 and HFC-900 is ascribed to the temperature increase in calcination. Though the content is very low, the carried N element in HDC is critical as a heteroatom to inspire new defects.[20] Fig. 5(b–e) illuminates the high-resolution spectra from the Fe 2p, C 1s, O 1s, and N 1s peaks of HFC-700. The γ-Fe_2O_3 and Fe_3O_4 are extremely similar under XRD measurements, so XPS analysis is necessary to verify the valence states of Fe element in Fe_3O_4. The Fe 2p peak is situated at 723.5 eV and 710.80 eV, corresponding to Fe 2p1/2 and Fe 2p3/2 (Fig. 5(b)), which fully confirms the existence of Fe_3O_4 in composites, instead of γ-Fe_2O_3. Fig. 5(c) depicts the C 1s spectra. Here, three deconvoluted peaks at the bonding energies of 288.40 eV, 286.40 eV and 284.40 eV are related to C═O, C–O and C–C/C═C groups, indicating four different species of C in the HFC-700. Besides, the O 1s peak located at 532.70 eV, 531.40 eV and 530.20 eV are responsible for the O–H, C–O/C═O and Fe–O groups, as can be seen in Fig. 5(d). The inherent O element in BDC can generate more defects, which is beneficial for microwave absorption. The N–C–N and N–H peaks of the N 1s level are centered at 401.30 eV and 400.20 eV in Fig. 5(f). The N element will enhance the surface interaction between HDC and SA-derived carbon, then facilitate the bonding forces, chemical and mechanical stability between them.[35] Beyond that, the N element plays the same role as the O element in defect generation.

It is commonly known that the magnetic properties of absorbers play vital roles in microwave absorption due to the magnetic loss behavior and these properties of the as-made composites were measured by VSM at room temperature, as shown in Fig. 6 (inset: closer inspection at low field). Four tested samples exhibited typical magnetic hysteresis loops with S-shaped curves. Unquestionably, the magnetization values mainly come from the Fe_3O_4 in these samples. The saturation magnetization (M_S), coercivity (H_C) and remanent magnetization (M_r) are displayed in Table S2.† The magnetization curves of FC-700 basically coincide with that of HFC-700, seemingly proving that the HDC has no effect on the magnetic properties. Due to its amorphous carbon matrix with plentiful defects, as described by the highest I_D/I_G value (1.76) and the largest specific surface area (628 m^2 g^{-1}), the HFC-800 manifests the lowest M_S and M_r value.[36,37] Numerous disordered atoms originating from defects decrease the magnetic moment, and the HFC-800 gives negligible M_S. Contrary to this, the HFC-900 reveals the highest M_S value and the lowest H_C value, which are due to the greater structural bulk.[38] The comparatively higher H_C of FC-700, HFC-700 and HFC-900 imply larger magneto-crystalline anisotropy, which would benefit microwave absorption.[24,39]

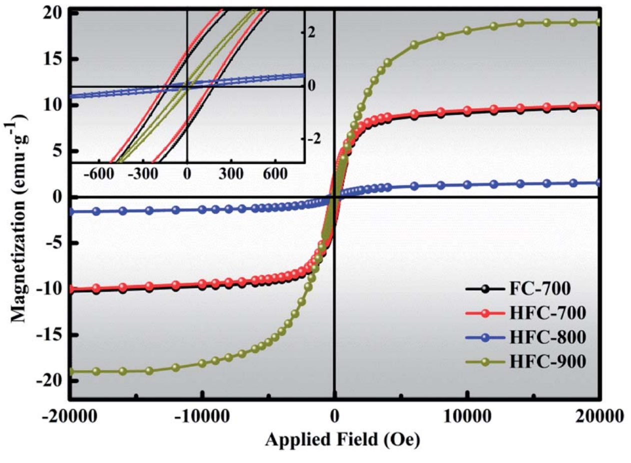

Fig. 6 Magnetization curves of FC-700, HFC-700, HFC-800 and HFC-900.

Electromagnetic parameters (ε', ε'', μ' and μ'') of FC-700, HFC-700, HFC-800 and HFC-900 were measured by a vector network analyzer at room temperature with a filler loading ratio of 35% in paraffin matrix, and the frequency ranges from 2 to 18 GHz. As is known, the relative complex permittivity ($\varepsilon_r = \varepsilon' - j\varepsilon''$) and permeability ($\mu_r = \mu' - j\mu''$) determine the microwave absorption performance.[40] Usually, the real parts of the complex permittivity (ε') and permeability (μ') correspond to the storage capability of electric and magnetic energy, while the imaginary parts (ε'' and μ'') represent the dissipation capability of electric and magnetic energy.[41] Fig. 7 depicts the ε', ε'', μ' and μ'' of all samples depending on frequency. An interesting finding in Fig. 7(a and b) is that both the ε' and ε'' of HFC-700 are higher than those of FC-700, exactly explaining the special function of HDC in permittivity enhancement and this allows better energy storage and dissipation. This enhancement owes much to the additional interface polarization brought by HDC and accompanying space charges.[34] For HFC-800 and HFC-900, which were obtained at higher temperatures, HDC almost disappeared due to high-temperature pyrolysis; the coked carbonaceous matrix ultimately acts as a dielectric material. After coking, the carbonaceous matrix with loose network structure became nubby and dense, which could lead to the improvement of dielectric parameters. At the frequency region of 2–15 GHz, the values of ε' and ε'' are in ascending order as follows: HFC-700, HFC-800 and HFC-900, indicating that with the carbonization temperature increasing, ε' and ε'' values also tend to increase. Overall, the ε' values of the HFC-X composites decrease successively with frequency increase, and this phenomenon can be seen in many papers. Li *et al.* pointed out that it arises from a frequency dispersion for samples, which could provide good impedance matching of incident microwaves.[42] In the high-frequency region (12–18 GHz), the ε'' values of HFC-X composites have several violent changes, which could be ascribed to the enhanced polarization relaxation.[43]

The μ' of HFC-X samples shown in Fig. 7(c) are almost constant around 1.05 over the 2–18 GHz without comparatively drastic fluctuation. The μ' value of FC-700 drops sharply from 1.3 to 0.7 at the frequency region of 9.5–11.5 GHz, and then climbs until the frequency reaches to 18 GHz; the μ' value of

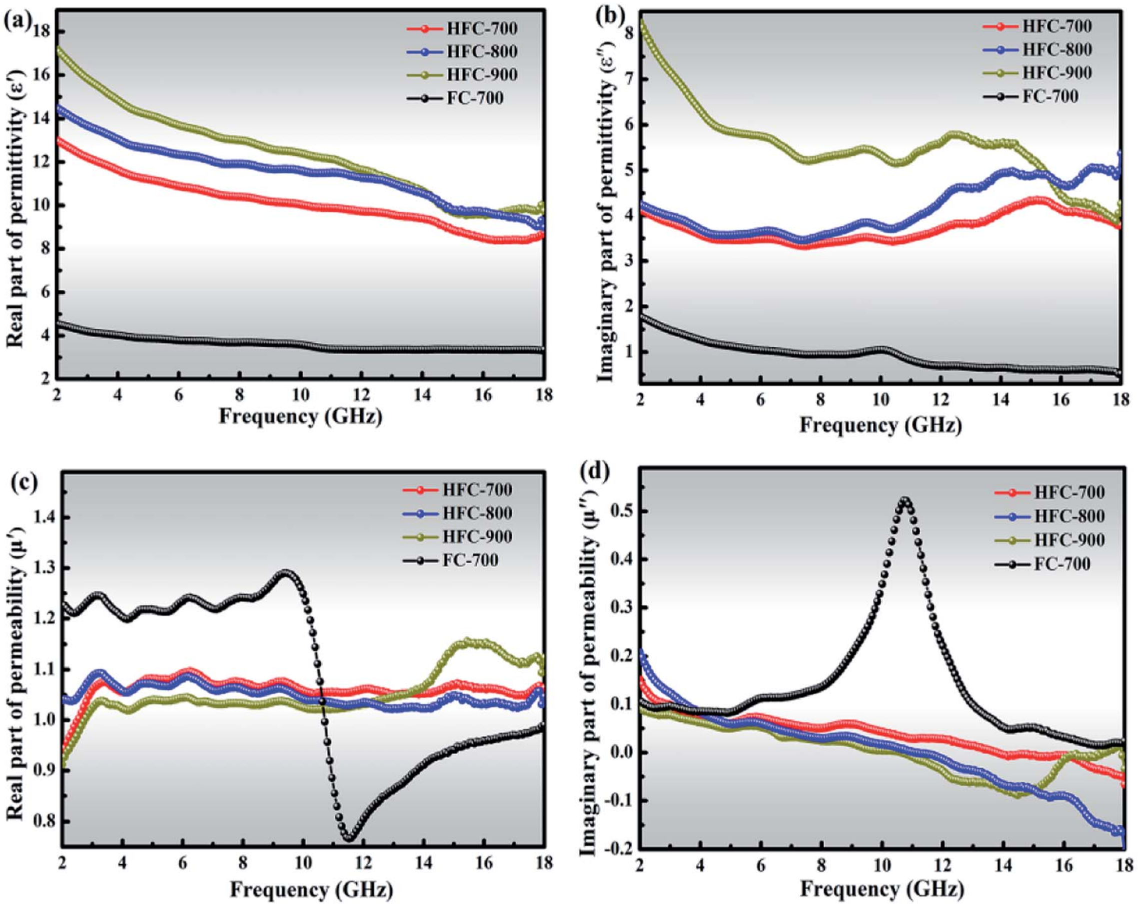

Fig. 7 Frequency dependence of the real (a) and imaginary (b) parts of relative complex permittivity, and the real (c) and imaginary (d) parts of the relative complex permeability of FC-700, HFC-700, HFC-800 and HFC-900.

HFC-900 also presents obvious fluctuations in high frequency, which might be attributable to the response in high-frequency electromagnetic field, resulting in resonance peaks.

Fig. 7(d) exhibits the μ'' values of all as-prepared samples. All the μ'' values of the HFC-*X* composites gently decrease around 0, implying that the natural resonance occurred in the systems,[44] yet the μ'' value of FC-700 has an apparent resonance peak at about 11 GHz, which is in agreement with the position of the corresponding mutation in Fig. 7(c). The strong resonance signal of FC-700 is mainly attributed to the magneto-crystalline anisotropic field, which is related to the geometric structures from various shapes of Fe_3O_4 nanoparticles. For HFC-700, HFC-800 and HFC-900, despite the same existence of irregular magneto-crystalline Fe_3O_4, the additional highly graphitized HDC in HFC-700, or the coking and aggregate carbon matrix of HFC-800 and HFC-900 hinder the ordered orientation of magnetic domains in magnetic crystals when loading the electromagnetic field, and thus, there are no obvious resonance peaks in the HFC-*X* composites. In general, the resonance peak means good dissipation capability of magnetic energy and further facilitates the microwave absorption, but the improvement of individual magnetic properties cannot control the microwave absorption performance completely.[2]

Fig. 8 plots the Cole–Cole curves of FC-700, HFC-700, HFC-800 and HFC-900, and a single semicircle corresponds to a Debye relaxation process.[45,46] Apparently, the quantity of distinguishable semicircles in any HFC-*X* as-made samples is more than that of

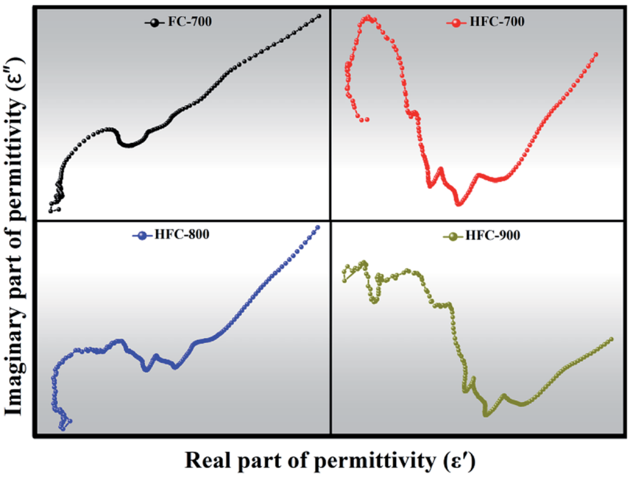

Fig. 8 Cole–Cole semicircles (ε *versus* ε') of FC-700, HFC-700, HFC-800 and HFC-900.

FC-700, which indicates more relaxation processes in HFC-*X* composites.[47] The relaxation process originates from the heterogeneous interfaces that exist between Fe_3O_4 and SA-derived carbon, Fe_3O_4 and HDC, HDC and SA-derived carbon, void and solid. This phenomenon appears in the heterogeneous media with different dielectric constants and conductivities, due to the accumulation of charges at the interfaces and the formation of dipoles.[48,49] The inherent heteroatoms like O and N elements in SA-derived carbon and HDC, as well as defects, can act as polarization centers to generate electron polarization relaxation. The HDC coupled with extra Debye relaxation processes help the HFC-*X* samples stand out easily.

The loss parameters can be evaluated in terms of dielectric tangent loss ($\tan\delta_\varepsilon = \varepsilon''/\varepsilon'$) and magnetic tangent loss ($\tan\delta_\mu = \mu''/\mu'$). As shown in Fig. 9(a), all the HFC-*X* samples present higher dielectric tangent loss than FC-700 over almost all the frequency range. As discussed above, this enhancement, benefiting from HDC, can greatly improve the microwave absorption. Fig. 9(b) displays the magnetic tangent loss of samples. Contrary to the dielectric tangent loss, FC-700 gives higher magnetic tangent loss than those of HFC-*X* samples. Notably, a sharp and strong magnetic loss peak located at 11 GHz for FC-700 is observed, which coincides with the peak of μ'' as shown in Fig. 7(d). As mentioned above, the uncommon peak of FC-700 is derived from the geometric anisotropy of Fe_3O_4 and unhindered magnetic domain orientation in the electromagnetic field. It is generally believed that the magnetic loss mainly originates from the domain wall resonance, hysteresis, natural resonance, and eddy current loss.[3,50] The hysteresis loss is derived from repeated magnetization and is negligible in a weak applied field, and the domain wall resonance loss only occurs in multidomain materials at much lower frequency (MHz), so these two types of magnetic loss can be excluded from this paper.[51,52] Thus, the natural resonance and eddy current loss are considered as the dominating loss mechanisms for ferromagnetic absorbers in the frequency range of 2–18 GHz. The eddy current effect can be expressed by the following:

$$C_o = \mu''(\mu')^{-2}f^{-1} \tag{1}$$

According to the equation, if the magnetic loss solely results from eddy current loss, the values of $\mu''(\mu')^{-2}f^{-1}$ should remain constant with respect to frequency.[53] Both FC-700 and HFC-*X* samples exhibit descending plots of $\mu''(\mu')^{-2}f^{-1}$ values in the low frequency from 2 to 4 GHz, as plotted in Fig. 9(c). This is contrary to the eddy current loss mechanism, suggesting that the natural resonance loss may be the main contributor under low frequency.[54] After 4 GHz, the $\mu''(\mu')^{-2}f^{-1}$ values of HFC-*X* samples slightly change around 0 without obvious fluctuation,

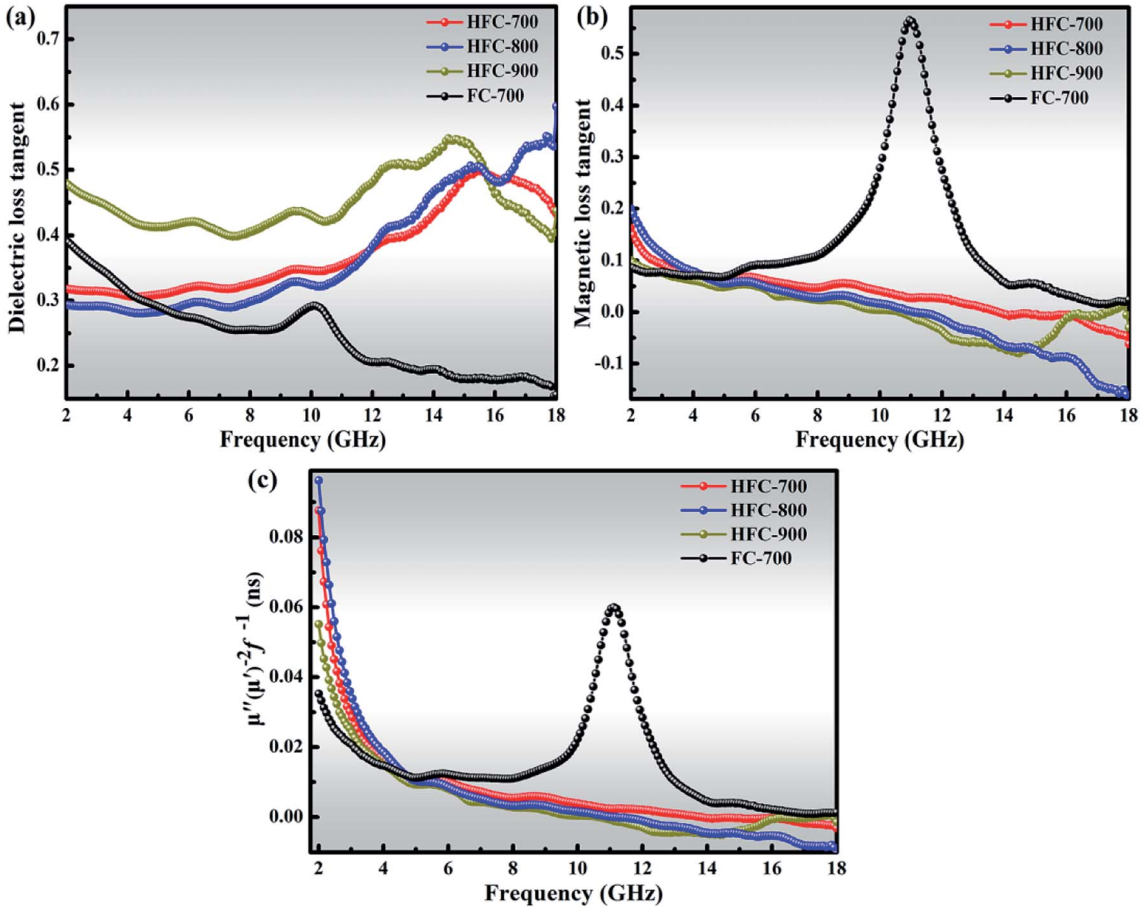

Fig. 9 Dielectric loss tangent (a), magnetic loss tangent (b) and $\mu''(\mu')^{-2}f^{-1}$ (c) of as-prepared samples.

and it can be deduced that the results may come from eddy current loss. Nonetheless, FC-700 presents a distinct peak at 11.5 GHz, which also falls into the natural resonance loss. From the obtained findings, one can conclude that HDC introduced the eddy current loss mechanism into the HFC-*X* series on the basis of natural resonance loss, while the magnetic loss of FC-700 was only due to natural resonance loss.

According to the transmission line theory, impedance matching and the attenuation constant (α) play decisive roles in the ultimate performance of microwave absorption. Microwave absorption is a joint outcome of dielectric loss and magnetic loss, and the impedance matching is an indicator to evaluate the degree of the synergistic effect between relative complex permittivity and permeability. Fig. 10(a) displays the values of the normalized characteristic impedance ($Z = |Z_{\text{in}}/Z_0|$), which were calculated from eqn (2) and (3).[3]

$$Z_{\text{in}} = Z_0(\mu_r/\varepsilon_r)^{1/2}\tanh[j(2\pi fd/c)(\mu_r\varepsilon_r)^{1/2}] \tag{2}$$

$$\text{RL (dB)} = 20\log|(Z_{\text{in}} - Z_0)/(Z_{\text{in}} + Z_0)| \tag{3}$$

Here, Z_{in} represents the impedance of free space while Z_0 corresponds to input characteristic impedance, c is the velocity of microwaves in free space and d is the thickness of the absorber. When the impedance matching ratio Z is equal to 1, microwaves will efficiently enter the microwave absorber to be further attenuated instead of reflected on the air/absorber interface.[41] As is shown in Fig. 10(a), when the thickness of all samples is 1.5 mm, HFC-700 presents the ideal impedance matching ratio, which is 1 at 17.52 GHz, and the Z values of HFC-800 and HFC-900 are a bit lower than that of HFC-700. For FC-700, its impedance matching ratio Z is far lower than 1 over the whole frequency range, which means poor microwave absorption of FC-700. Moreover, the attenuation constant (α) is another key factor to quantify the capability of microwave absorption when taking account of permeability and permittivity parameters; its expression is as follows:[54]

$$\alpha = (\sqrt{2}\pi f/c) \times \sqrt{[(\mu''\varepsilon'' - \mu'\varepsilon') + \sqrt{[(\mu''\varepsilon'' - \mu'\varepsilon')^2 + (\mu''\varepsilon'' + \mu'\varepsilon')^2]}]} \tag{4}$$

As is known, a higher attenuation constant signifies that much of the entered microwave will be attenuated and transformed into thermal energy. It can be seen in Fig. 10(b) that HFC-700 always creates a higher attenuation constant than any other samples during all the frequency variation. The wonderful behavior in both impedance matching and attenuation constant can directly explain the best absorption performance of HFC-700 when compared with other products.

To gain insight into the microwave absorption ability of the as-made samples, reflection losses RL (dB) with different absorbing thickness were deduced from eqn (2) and (3); the frequency dependence of RL curves with the incremental thickness of all products is shown in Fig. 11. Generally, a RL value under −10 dB means more than 90% of microwaves will be absorbed, and the corresponding microwave absorber can be employed for actual applications. It can be observed in Fig. 11 that the four products based on SA-derived carbon all present RL peaks under −10 dB, confirming that the 3D hierarchical network structure of SA-derived carbon facilitates microwave absorption. Interfacial polarization, multiple reflections and scattering originating from numerous pores in the 3D network structure effectively improve the ability for microwave absorption. It is easy to identify from Fig. 11(b) that HFC-700 has, so far, performed the best as the RL. Its minimal RL is −50.80 dB at 17.52 GHz with a thin thickness of 1.5 mm, corresponding to an effective absorption (<−10 dB) bandwidth of 3.52 GHz from 14.48 to 18 GHz. Furthermore, the effective absorption bandwidth of HFC-700 can be adjusted at the frequency region of 8.24 to 18 GHz by tuning the thickness between 1.5 and 2.5 mm. However, FC-700 only presents five feeble RL peaks under −10 dB, with a relatively thicker thickness from 3.0 to 5.0 mm and the minimal RL is −31.32 dB. By this comparison, the topping behavior in the microwave absorption of HFC-700 elucidates an indelible function of HDC. As previously mentioned, the HDC decorated on the 3D network of the carbonaceous matrix tremendously improves the absorption performance of materials. As the carbonization temperature increased, the microwave absorption performances of HFC-800 and HFC-900 decreased successively, due to the destruction of the network structure. Despite this, the abilities of HFC-800 and HFC-900 in

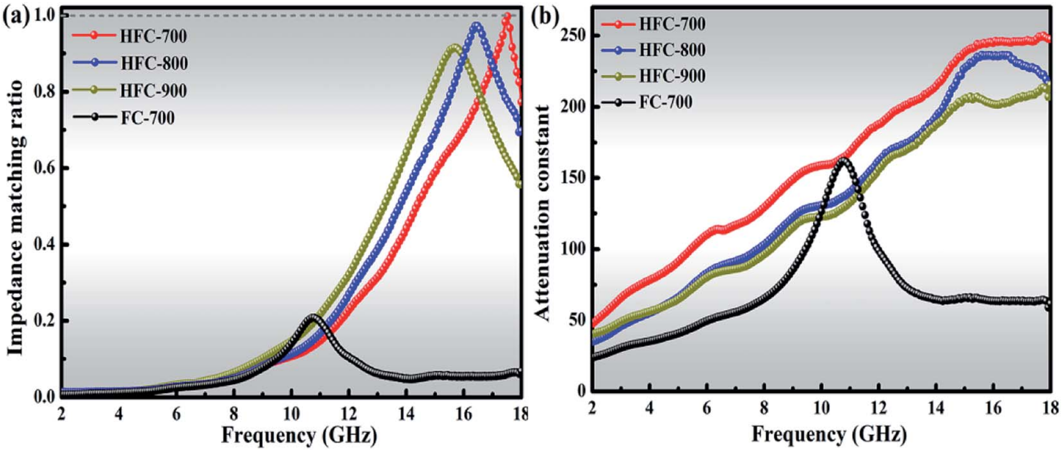

Fig. 10 The impedance matching ratio of the products at a thickness of 1.5 mm (a); attenuation constant of as-made composites (b).

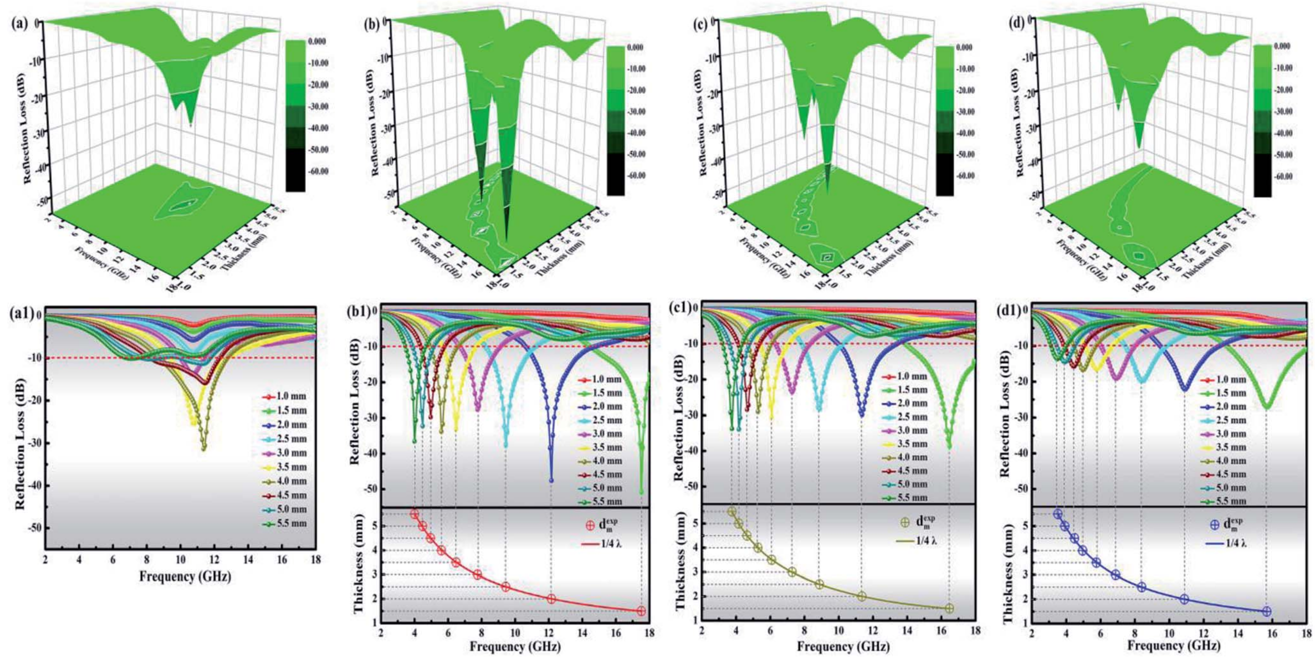

Fig. 11 3D images of calculated RL values and RL curves of FC-700 (a and a1), HFC-700 (b and b1), HFC-800 (c and c1) and HFC-900 (d and d1). The bottoms of (a1–c1) are emulations of the absorber thickness (d_m) *vs.* peak frequency (f_m) for HFC-700, HFC-800 and HFC-900 under the $\lambda/4$ model.

microwave absorption still meet the practical application requirements when compared with FC-700. As observed in Fig. 11(b1–d1), in the wake of the layer thickness varying from 1.0 to 5.5 mm, all the HFC-*X* composites showed splendid frequency dispersion that completely covered the S-band (2–4 GHz), C band (4–8 GHz), X band (8–12 GHz) and Ku band (12–18 GHz). This implies that they may have useful applications in satellite communications, military radar systems and weather radar. Table 1 shows the microwave absorption properties in similar works that make use of biomass materials to prepare hierarchical structures with vast pores. In comprehensive contrast to the latest excellent published SA-derived absorbers, that is, the bimetallic porous Co_xNi_y/SA-derived carbon composite,[55] or the SA–Ni–(Fe_3O_4/CNT) absorber,[6] our as-prepared composite decorated by monometallic Fe^{3+} in this work is lighter and more efficient with strong absorption. By comparison, the microwave absorber produced by the current work has obvious advantages.

Like frequency, the thickness of the microwave absorber is another key factor in determining the practical application. In addition to the dielectric loss and magnetic loss from the absorber itself, the microwaves can also be attenuated by a "geometric effect", which is called the $\lambda/4$ matching theory.[30] This theory can be expressed by eqn (5):

$$d_m = n\lambda/4 = nc/[4f_m\sqrt{(|\varepsilon_r||\mu_r|)}]\ (n = 1, 3, 5,\ldots) \quad (5)$$

Here, λ is the wavelength of the microwave, d_m is the absorber thickness, f_m is the frequency of the absorption peak, c is the velocity of light in vacuum. Based on the l/4 matching model, if d_m and f_m meet the above equation, the phase difference between the incident and reflected microwaves on air/absorber

Table 1 Comparative studies on microwave absorbers prepared from biomass materials

Absorber	Content (wt%)	Min. RL (dB)	Thickness (mm)	<−10 dB bandwidth (GHz)	Ref.
Nano-porous carbon	30	−42.4	2.0	1.76	18
Heteroatom-doped carbon	30	−44.6	1.68	2.2	20
Carbon nanofiber	80	−36	2.0	5.4	56
$Ni(OH)_2$/carbon	50	−23.6	6.0	2.0	4
Wood-based absorber	—	−68.3	4.28	6.13	57
Porous Co_xNi_y/SA-derived carbon	50	−49.08	1.4	6.68	55
SA–Ni–(Fe_3O_4/CNT)	25	−32	2.0	3.2	6
Dopamine-derived cavities/Fe_3O_4/SA-derived carbon	**35**	**−50.8**	**1.5**	**3.5**	**This work**

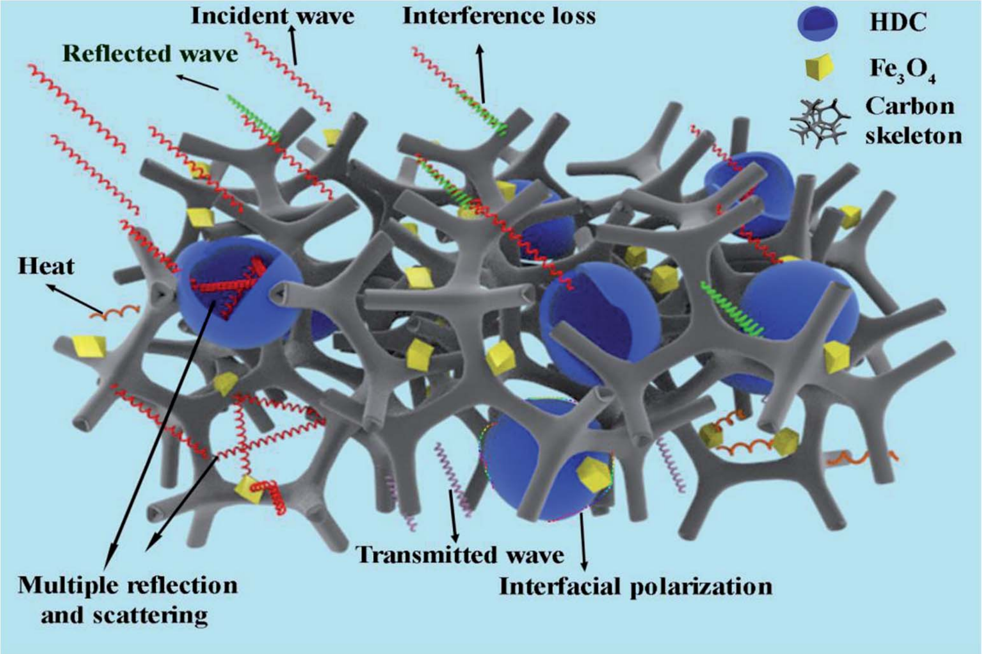

Scheme 2 Possible schematic of microwave absorption by the fabricated HFC-700 composite.

interface is 180°, causing a cancellation effect (also named interference loss), by which the two microwaves cancel each other out.[8,58] The bottoms of Fig. 11(a1–c1) are plots of the absorber thickness (d_m) *vs.* peak frequency (f_m) for HFC-700, HFC-800 and HFC-900, respectively, where d_m^{exp} represents the experimental thicknesses and the smooth curves are emulated from the $\lambda/4$ model. It is apparent that all the d_m^{exp} are exactly located at the $\lambda/4$ curve, signifying that the absorption thickness and frequency of HFC-*X* composites entirely obey the $\lambda/4$ model. That is to say, the cancellation effect happened in HFC-*X* samples rather than FC-700. On the other hand, the $\lambda/4$ matching theory is an efficient guide for the design of absorption material with appropriate thickness once the required complex permeability and permittivity are obtained.

Given the abovementioned analysis, the optimal microwave absorption of HFC-700 can be attributed to several proposed mechanisms. To give a visual demonstration of the absorption mechanisms, an understandable schematic diagram is presented in Scheme 2. Due to the combined effects of permittivity and permeability, the improved impedance matching prompts microwaves to enter the absorber as much as possible. Only a small amount of microwaves is reflected or cancelled out due to interference loss. Abundant defects, as well as porous channels and cavities provided by the unique 3D network structure decorated by HDC, can act as activated sites in favor of multiple reflections and scattering, after which, the incident wave will be effectively attenuated and transformed into thermal energy. Moreover, the additional eddy current loss associated with HDC and the native natural resonance loss are also profitable for dissipating the incident wave. Furthermore, diverse heterogeneous interfaces (Fe_3O_4–carbon, Fe_3O_4–HDC, HDC–carbon and void–solid) can cause interfacial polarization, followed by the polarization loss of microwaves.

Conclusion

The current study has unveiled an excellent microwave absorber with unique 3D network structure derived from biomass SA, in which the HDC and dispersed Fe_3O_4 nanoparticles are evenly decorated. The fascinating 3D porous structure is helpful for multiple reflections and scattering of the incident wave; the additional HDC markedly elevated the permittivity properties of HFC-*X* samples. The meticulous cooperative effects of HDC, the SA-derived carbon network and magnetic Fe_3O_4 nanoparticles are of paramount importance in microwave absorption, by which strong reflection losses, ultra-wide response bands, and thin matched thicknesses were realized together. It is firmly believed that these novel hollow dopamine-derived cavities/Fe_3O_4 nanoparticles-encapsulated carbonaceous composites with admirable microwave absorption performance and simple feasible preparation would be practical candidates for preventing electromagnetic pollution. Moreover, this type of 3D network structure of seaweed-derived carbon can be used in further functional design and applications.

Conflicts of interest

The authors declare that they have no conflict of interest.

Acknowledgements

This project was financially supported by the National Key R&D Program of China (2017YFB0308701), the National Natural Science Foundation of China (21676039), State Key Laboratory of Bio-Fibers and Eco-Textiles (2017kfkt12) and Innovative Talents in Liaoning Universities and Colleges (LR2017045) are highly appreciated.

References

1 X. A. Li, D. X. Du, C. S. Wang, H. Y. Wang and Z. P. Xu, *J. Mater. Chem. C*, 2018, **6**, 558–567.

2 L. C. Jia, D. X. Yan, X. F. Liu, R. J. Ma, H. Y. Wu and Z. M. Li, *ACS Appl. Mater. Interfaces*, 2018, **10**, 11941–11949.

3 B. Zhao, X. Q. Guo, W. Y. Zhao, J. S. Deng, G. Shao, B. B. Fan, Z. Y. Bai and R. Zhang, *ACS Appl. Mater. Interfaces*, 2016, **8**, 28917–28925.

4 H. T. Guan, H. Y. Wang, Y. L. Zhang, C. J. Dong, G. Chen, Y. D. Wang and J. B. Xie, *Appl. Surf. Sci.*, 2018, **447**, 261–268.

5 B. Liao, Z. J. An and J. J. Zhang, *RSC Adv.*, 2017, **7**, 21721–21732.

6 N. Zhou, Q. D. An, Z. Y. Xiao, S. R. Zhai and Z. Shi, *ACS Sustainable Chem. Eng.*, 2017, **5**, 5394–5407.

7 M. Q. Ning, J. B. Li, B. Y. Kuang, C. Z. Wang, D. Z. Su, Y. J. Zhao, H. B. Jin and M. S. Cao, *Appl. Surf. Sci.*, 2018, **447**, 244–253.

8 R. W. Shu, G. Y. Zhang, X. Wang, X. Gao, M. Wang, Y. Gan, J. J. Shi and J. He, *Chem. Eng. J.*, 2018, **337**, 242–255.

9 L. Y. Zhu, X. J. Zeng, M. Chen and R. H. Yu, *RSC Adv.*, 2017, **7**, 26801–26808.

10 I. Arief, S. Biswas and S. Bose, *ACS Appl. Mater. Interfaces*, 2017, **9**, 19202–19214.

11 Y. H. Zhan, J. Wang, K. Y. Zhang, Y. C. Li, Y. Y. Meng, N. Yan, W. K. Wei, F. B. Peng and H. S. Xia, *Chem. Eng. J.*, 2018, **344**, 184–193.

12 F. Wu, Q. Zeng, Y. L. Xia, M. X. Sun and A. M. Xie, *Appl. Phys. Lett.*, 2018, **112**, 192902.

13 W. S. Hummers and R. E. Offeman, *J. Am. Chem. Soc.*, 1958, **80**, 1339.

14 P. Liu, J. Yan, X. Gao, Y. Huang and Y. Zhang, *Electrochim. Acta*, 2018, **272**, 77–87.

15 Y. H. Zou, X. F. Yang, C. X. Lv, T. C. Liu, Y. Z. Xia, L. Shang, G. I. N. Waterhouse, D. J. Yang and T. R. Zhang, *Adv. Sci.*, 2017, **4**, 1600262.

16 Y. Z. Yan, Q. D. An, Z. Y. Xiao, S. R. Zhai, B. Zhai and Z. Shi, *J. Mater. Chem. A*, 2017, **5**, 17073–17087.

17 Y. N. Gong, D. L. Li, C. Z. Luo, Q. Fu and C. X. Pan, *Green Chem.*, 2017, **19**, 4132–4140.

18 X. Qiu, L. X. Wang, H. L. Zhu, Y. K. Guan and Q. Zhang, *Nanoscale*, 2017, **9**, 7408–7418.

19 S. S. Gao, Q. D. An, Z. Y. Xiao, S. R. Zhai and Z. Shi, *RSC Adv.*, 2018, **8**, 19011–19023.

20 S. K. Singh, H. Prakash, M. J. Akhtar and K. K. Kar, *ACS Sustainable Chem. Eng.*, 2018, **6**, 5381–5393.

21 F. Wang, Y. Sun, D. Li, B. Zhong, Z. Wu, S. Zuo, D. Yan, R. Zhuo, J. Feng and P. Yan, *Carbon*, 2018, **134**, 264–273.

22 Y. N. Wang, Z. L. Zhou, M. G. Chen, Y. X. Huang, C. X. Wang and W. L. Song, *Appl. Surf. Sci.*, 2018, **439**, 176–185.

23 F. Wu, A. M. Xie, M. X. Sun, Y. Wang and M. Y. Wang, *J. Mater. Chem. A*, 2015, **3**, 14358–14369.

24 H. L. Lv, X. H. Liang, G. B. Ji, H. Q. Zhang and Y. W. Du, *ACS Appl. Mater. Interfaces*, 2015, **7**, 9776–9783.

25 K. Wang, G. P. Wan, G. L. Wang, Z. Y. He, S. H. Shi, L. H. Wu and G. Z. Wang, *J. Colloid Interface Sci.*, 2018, **511**, 307–317.

26 J. Y. Fu, W. Yang, L. Q. Hou, Z. Chen, T. Qiu, H. T. Yang and Y. F. Li, *Ind. Eng. Chem. Res.*, 2017, **56**, 11460–11466.

27 Y. Wang, F. Q. Gu, L. J. Ni, K. Liang, K. Marcus, S. L. Liu, F. Yang, J. J. Chen and Z. S. Feng, *Nanoscale*, 2017, **9**, 18318–18325.

28 Y. N. Zhang, B. Quan, W. Liu, X. H. Liang, G. B. Ji and Y. W. Du, *Dalton Trans.*, 2017, **46**, 9097–9102.

29 K. Manna and S. K. Srivastava, *ACS Sustainable Chem. Eng.*, 2017, **5**, 10710–10721.

30 Y. L. Zhou, J. Muhammad, X. F. Zhang, D. X. Wang, Y. P. Duan, X. L. Dong and Z. D. Zhang, *RSC Adv.*, 2018, **8**, 6397–6405.

31 J. Li, D. Zhang, H. Qi, G. M. Wang, J. M. Tang, G. Tian, A. H. Liu, H. J. Yue, Y. Yu and S. H. Feng, *RSC Adv.*, 2018, **8**, 8393–8401.

32 H. L. Xu, X. W. Yin, M. Zhu, M. K. Han, Z. X. Hou, X. L. Li, L. T. Zhang and L. F. Cheng, *ACS Appl. Mater. Interfaces*, 2017, **9**, 6332–6341.

33 E. G. Luo, M. L. Xiao, J. J. Ge, C. P. Liu and W. Xing, *J. Mater. Chem. A*, 2017, **5**, 21709–21714.

34 Z. C. Wu, K. Tian, T. Huang, W. Hu, F. F. Xie, J. J. Wang, M. X. Su and L. Li, *ACS Appl. Mater. Interfaces*, 2018, **10**, 11108–11115.

35 X. He, P. R. Liu, J. Liu, Y. Muhammad, M. P. Zhu, J. H. Sun, X. M. Cui, D. K. Liao and Z. F. Tong, *J. Mater. Chem. B*, 2017, **5**, 9211–9218.

36 N. A. M. Barakat, M. F. Abadir, K. T. Nam, A. M. Hamza, S. S. Al-Deyab, W. Baek and H. Y. Kim, *J. Mater. Chem.*, 2011, **21**, 10957–10964.

37 N. Pathak, S. K. Gupta, C. L. Prajapat, S. K. Sharma, P. S. Ghosh, B. Kanrar, P. K. Pujari and R. M. Kadam, *Phys. Chem. Chem. Phys.*, 2017, **19**, 11975–11989.

38 X. H. Yan, G. J. Liu, M. Haeussler and B. Z. Tang, *Chem. Mater.*, 2005, **17**, 6053–6059.

39 C. Wang, X. J. Han, X. L. Zhang, X. R. Hu, T. Zhang, J. Y. Wang, Y. C. Du, X. H. Wang and P. Xu, *J. Phys. Chem. C*, 2010, **114**, 14826–14830.

40 L. N. Sha, P. Gao, T. T. Wu and Y. J. Chen, *ACS Appl. Mater. Interfaces*, 2017, **9**, 40412–40419.

41 X. Jian, X. Y. Xiao, L. J. Deng, W. Tian, X. Wang, N. Mahmood and S. X. Dou, *ACS Appl. Mater. Interfaces*, 2018, **10**, 9369–9378.

42 X. A. Li, B. Zhang, C. H. Ju, X. J. Han, Y. C. Du and P. Xu, *J. Phys. Chem. C*, 2011, **115**, 12350–12357.

43 J. Yan, Y. Huang, X. Han, X. Gao and P. Liu, *Composites, Part B*, 2019, **163**, 67–76.

44 N. Zhou, Q. D. An, W. Zheng, Z. Y. Xiao and S. R. Zhai, *RSC Adv.*, 2016, **6**, 98128–98140.

45 S. S. Dai, Y. Cheng, B. Quan, X. H. Liang, W. Liu, Z. H. Yang, G. B. Ji and Y. W. Du, *Nanoscale*, 2018, **10**, 6945–6953.

46 J. Yan, Y. Huang, C. Wei, N. Zhang and P. Liu, *Composites, Part A*, 2017, **99**, 121–128.

47 Y. Jiang, Y. Chen, Y. J. Liu and G. X. Sui, *Chem. Eng. J.*, 2018, **337**, 522–531.

48 S. He, G. S. Wang, C. Lu, J. Liu, B. Wen, H. Liu, L. Guo and M. S. Cao, *J. Mater. Chem. A*, 2013, **1**, 4685–4692.

49 K. F. Wang, Y. J. Chen, R. Tian, H. Li, Y. Zhou, H. A. Duan and H. Z. Liu, *ACS Appl. Mater. Interfaces*, 2018, **10**, 11333–11342.
50 W. Xu, Y. F. Pan, W. Wei, G. S. Wang and P. Qu, *Appl. Surf. Sci.*, 2018, **428**, 54–60.
51 M. Z. Wu, Y. D. Zhang, S. Hui, T. D. Xiao, S. H. Ge, W. A. Hines, J. I. Budnick and G. W. Taylor, *Appl. Phys. Lett.*, 2002, **80**, 4404–4406.
52 D. Ding, Y. Wang, X. D. Li, R. Qiang, P. Xu, W. L. Chu, X. J. Han and Y. C. Du, *Carbon*, 2017, **111**, 722–732.
53 G. M. Li, L. C. Wang, W. X. Li, R. M. Ding and Y. Xu, *Phys. Chem. Chem. Phys.*, 2014, **16**, 12385–12392.
54 P. Wang, L. F. Cheng, Y. N. Zhang and L. T. Zhang, *ACS Appl. Mater. Interfaces*, 2017, **9**, 28844–28858.
55 B. Quan, X. Liang, G. Ji, Y. Zhang, G. Xu and Y. Du, *ACS Appl. Mater. Interfaces*, 2017, **9**, 38814–38823.
56 X. L. Wang, X. Huang, Z. R. Chen, X. P. Liao, C. Liu and B. Shi, *J. Mater. Chem. C*, 2015, **3**, 10146–10153.
57 J. Xi, E. Zhou, Y. Liu, W. Gao, J. Ying, Z. Chen and C. Gao, *Carbon*, 2017, **124**, 492–498.
58 L. Liu, Z. D. He, Y. T. Zhao, J. C. Sun and G. X. Tong, *J. Alloys Compd.*, 2018, **765**, 1218–1227.